Volume 1 | Number 1 | Jan 2013 | Pages 1–100

Journal of
Materials Chemistry A

Materials for energy and sustainability
www.rsc.org/materialsA

ROYAL SOCIETY
OF CHEMISTRY

www.rsc.org/materialsA

Two-Dimensional Heterostructures of V_2O_5 Nanosheets and Reduced Graphene Oxide as Electrodes for High Energy Density Asymmetric Supercapacitors

D. H. Nagaraju, Qingxiao Wang, P. Beaujuge, and H. N. Alshareef[*]

Materials Science and Engineering, King Abdullah University of Science & Technology (KAUST), Thuwal 23955-6900, Saudi Arabia

E-mail: husam.alshareef@kaust.edu.sa

ABSTRACT

In this article, we report the synthesis of electrode materials based on two-dimensional (2D) heterostructures of V_2O_5 nanosheets (V_2O_5 NS) and reduced graphene oxide (rGO) electrodes for *asymmetric* supercapacitor applications.. Specifically, the 2D V_2O_5 and rGO/V_2O_5 nanosheet electrodes showed a specific capacitance of 253 F/g and 635 F/g, respectively at a current density of 1 A/g. The capacitance of the heterostructures is almost 2.5 times times higher than the 2D V_2O_5 nanosheets alone. The corresponding energy density of 39 Wh/kg and 79.5 Wh/kg were achieved for the same two electrodes at a power density of 900 W/kg in asymmetric supercapacitor configuration. The energy and power density using the nanosheet heterostructure are, to our knowledge, higher than any that have been previously reported for asymmetric supercapacitors using V_2O_5 electrodes.

Keywords: 2D Materials, Reduced Graphene Oxide, V_2O_5 Nanosheets, Heterostructures, Asymmetric Supercapacitor

1. Introduction

Among the various energy storage devices, supercapacitors have recently received considerable research interest because they can complement or replace batteries in a variety of applications. Supercapacitors, also known as ultracapacitors, store electrical energy by two mechanisms. One mechanism is similar to conventional double layer capacitors that involve electrostatic adsorption of opposite charges at the electrode-electrolyte interface. The other mechanism is based on electrochemical reactions that involve psuedocapacitive materials such as metal oxides and conducting polymers.

Recently, much of the work has been focused on improving the energy density of supercapacitors either by increasing surface area or by improving the redox activity.[1-6] As the energy density is proportional to square of the voltage ($E = \frac{1}{2} CV^2$), increasing the operating voltage window could result in the higher energy density supercapacitors. As the aqueous electrolytes have the stable potential window only up to 1.23 V, organic electrolytes are being employed for the higher operating voltage windows. Although higher working voltage windows have been achieved using organic electrolytes, their commercial practical energy densities are very low (5-6 Wh kg^{-1}). This has prevented their widespread use. In addition, they are also known for their flammability, lower ionic conductivity, overcharging, and short circuiting effect.[7] Hence, the quest for exploring less expensive aqueous energy storage devices which are environment friendly, could serve the future demand in high energy density supercapacitors. In addition, aqueous electrolytes possess better ionic conductivity, higher capacitance, and superior safety compared to the non-aqueous electrolytes. The energy densities of the aqueous supercapacitors have been significantly increased using asymmetric device configuration. A vast variety of materials have been investigated as a cathode material for fabricating asymmetric supercapacitors, which include nanostructured carbonaceous materials, polymers, and transition

metal oxides.[8-18] In particular, considerable research attention has been focused on metal oxides [1, 19-23] due to ease of preparation with controllable nanostructured morphology and their fast reversible Faradaic reactions, which result in relatively high energy density.

Among the various metal oxides, V_2O_5 has a layered structure and possess mixed valence state, which makes it a versatile material for pseudocapacitor applications.[24-44] The nanostructures of V_2O_5 plays major role in delivering a high energy density. The nanostructures of V_2O_5 such as nanowires,[25] nanoribbons,[26] nanosheets[27] etc. have been extensively explored for supercapacitor applications. However, the number of reports on using 2D V_2O_5 electrodes for supercapacitor, applications, especially in asymmetric device configuration, is still very small. For example, X. Rui *et al*. have prepared the hydrated V_2O_5 NS by sol-gel technique and used them in organic electrolyte supercapacitors.[27] J. Zhu *et al*. have synthesized the 3D nanostructures of V_2O_5 NS by freeze drying technique and shown the symmetrical device characteristics.[45] In this study, we have designed 2D heterostructures based on rGO and V_2O_5 nanosheet heterostructures, where the rGO nanosheets facilitate electron transfer in supercapacitor electrodes, giving rise to higher energy density and power densities than any previously reported V_2O_5 based asymmetric supercapacitive devices. The energy and power density values we obtained are, to our knowledge, higher than any that have been previously reported for asymmetric supercapacitors using V_2O_5 electrodes.

2. Experimental

2.1. Synthesis of GO

Graphite oxide was synthesized from graphite by modified Hummers method. Briefly, 2g of graphite powder and 1g $NaNO_3$ were mixed with 96 mL of conc. H_2SO_4 under ice cold condition. To this, 6 g of $KMnO_4$ was added in portions under vigorous stirring and temperature of the solution was kept below 10 °C using ice bath. The reaction mixture was stirred for 24

hours at 35 °C by removing the ice bath. To this, slowly add 400 mL of water and followed by 5 mL of 30% H_2O_2. The solution was stirred for another 2 h, filtered and washed with 10% HCl followed by water. Final product was dried at 80 °C for about 24 hours. GO was prepared by sonication the 3 mg of graphite oxide in 1 mL of water for about 30 minutes.

2.2. Synthesis of reduced graphene oxide (rGO)

The pH of the 200 mL of GO solution was adjusted to 10 using ammonia solution. To this 50 μl of hydrazine hydrate was added and stirred at 60 °C for 2 hours. The resulting rGO was filtered and washed several times with water and dried. The rGO was activated by treating with 7 M KOH followed by washed with water and heated under argon atmosphere for 2 hours at 800 °C.

2.3. Synthesis of 2D V_2O_5 NS and rGO/V_2O_5 NS

In a typical synthesis, the bulk V_2O_5 material was prepared by heating ammonium metavanadate at 400 °C for 2 hours in air. The resulting, V_2O_5 powder was dissolved in minimum amount of aqueous hydrogen peroxide solution and stirred until to obtain clear orange red colored solution. The clear orange red colored solution was transferred to the 50 mL of Teflon-lined autoclave which was sealed and heated at 180 °C for 24 hours. The solution was cooled to room temperature and precipitate was collected by centrifugation and washed with water, dried in air at 80 °C for 24 hours. The rGO/V_2O_5 NS was obtained by mixing the equal volume ratio of the bulk V_2O_5 solution and GO and above hydrothermal procedure was repeated. The V_2O_5 NS and rGO/V_2O_5 NS were characterized by X-ray diffraction (Bruker, D8-Advance XRD, Cu Kα, λ = 1.5406 Å). The morphology of the materials was investigated by scanning electron microscopy (FEI Helios NanoLab, 5 kV) and transmission electron micrograph (FEI Titan).

2.4. Electrodes Preparation

The V_2O_5 NS and rGO/V_2O_5 NS were mixed with acetylene black and polytetrafluoroethylene (PTFE) binder in a weight ratio of 85:10:5 in ethanol using ultrasonicator for 30 minutes. The ethanolic solution was drop coated on a carbon paper substrate (ELAT, Nuvant systems Inc.) followed by drying at $80\ ^0C$ for about 24 hours. The mass loading of the sample is about 0.5 mg cm^{-2}. The electrochemical performance of the prepared electrodes were studied in 1 M KCl with three electrode configuration consisting of modified carbon cloth paper electrode as the working electrode, Pt wire as the counter electrode and Ag/AgCl (1 M KCl) as the reference electrodes, respectively. The cyclic voltammetry, galvanostatic charge-discharge cycling and electrochemical impedance measurements were performed using Biologic VMP3 machine.

3. Results and Discussion

3.1. Synthesis and Characterization of the V_2O_5 Based Layered Electrodes

Chemical synthesis was used to fabricate the 2D materials and electrode composites we evaluated in this study.   In particular, the structure and electrode morphology investigated are illustrated schematically in Figure 1. The bulk V_2O_5 powder (shown on left) was first chemically prepared as described in the experimental section. The V_2O_5 nanosheets was subsequently formed by hydrothermal exfoliation of the V_2O_5 powder (top) or by hydrothermal exfoliation a mixture of V_2O_5 and rGO (bottom). Further details are given in the methods section.

The structure of the 2D V_2O_5 nanosheets was investigated by X-ray diffraction (XRD). The XRD pattern (Figure 2a) shows several reflections corresponding to the (001), (003), (004) and (005) planes of V_2O_5 with orthorhombic structure (JCPDS no. 40-1296). The intensity of XRD peaks is significantly reduced for rGO/V_2O_5 NS, a result that could be due to the lower loading V_2O_5 NS.[45] The Raman scattering spectra (Figure 2b) of the V_2O_5 NS and rGO/V_2O_5 NS show peaks

at 95, 139.5, 192.5, 282.5, 406.8, 478, 525, 695.2 and 993 cm^{-1} which are characteristic peaks of

V_2O_5.[46] In addition to the V_2O_5 peaks, Raman spectra of rGO/V_2O_5 NS shows peaks at 1370 and

1670 cm^{-1} representing the D and G bands of graphene, and confirming the presence of graphene

sheets along with the V_2O_5 NS.

The D and G band peaks were fitted and analyzed to estimate the I_D/I_G ratio. Typically, the I_D/I_G

ratio was found to be 0.92 and 0.8 for rGO/V_2O_5 NS and GO respectively. The increased I_D/I_G

ratio indicating that the reduction process and graphitic ordering of sp^2 carbon clusters expected

for the rGO samples.[47] In addition, we have estimated the mean sp^2 crystallite sizes from the

formula L_a (nm) = $(2.4 \times 10^{-4}) \lambda^4 (I_D/I_g)^{-1}$ where, La = crystallite size, λ = wavelength and found

to be 12 nm.

Scanning electron microscopy (SEM) has been carried out to study the morphology of

V_2O_5 NS and rGO/V_2O_5 NS as shown in the Figure S4. The SEM images clearly show the

nanosheet morphology for V_2O_5 and the nanosheets are well dispersed in the rGO layers.

To obtain more insight into the morphology and local structure of the V_2O_5 NS and

rGO/V_2O_5 NS electrodes we used transmission electron microscopy (TEM) and scanning

transmission electron microscopy (STEM). Figure 3 shows the TEM images of V_2O_5 and

rGO/V_2O_5. The 2D nature of the V_2O_5 sheets and the composite can be clearly seen from these

images. The lateral dimensions of the nanosheets range from 80 to 200 nm. The high resolution

TEM (HRTEM) images of these sheets are shown in the insets of Fig. 3b and 3d, which display

the lattice fringes with a spacing of 1.15 nm, corresponding to the (110) planes of V_2O_5. The

diffraction pattern of rGO/V_2O_5 NS associated with the polycrystalline rings along with the

single crystalline dots of V_2O_5, confirms the presence of rGO along with the V_2O_5 NS.

To identify the rGO and V_2O_5 regions in the rGO/V_2O_5 NS, electron energy loss spectrum (EELS) was taken (Supporting information, Figure S1a). This EELS spectrum is characteristic of vanadium in the energy range of 500-560 eV, comprising of VL edges at 519 (L_{III}) and 526 (L_{II}) eV.[48] However, this same edge spectra in the region 500-560 eV was absent in regions that are dominated by rGO sheets (Supporting information, Figure S1b). STEM image and corresponding line spectra confirms the presence of carbon and vanadium (Supporting information, Figure S2). The electron diffraction patterns, EELs spectra, and STEM scans were taken from different regions of the composite and indicate that the composite is fairly homogeneously mixed.

To investigate the distribution of elements, elemental mapping was carried out using STEM. Figure 4 and 5 shows the STEM image of V_2O_5 NS and rGO/V_2O_5 NS and their corresponding (zoomed portion) EELS elemental mapping images. Elemental mapping of V_2O_5 NS indicates that the absence of carbon and presence of vanadium (red) and oxygen (blue). The green lines due to carbon from the elemental mapping originated from the carbon coated TEM copper grid. Elemental mapping of rGO/ V_2O_5 NS confirms the presence of carbon (green) of rGO and vanadium (red) and oxygen (blue) of V_2O_5 indicating that the V_2O_5 NS are associated with rGO sheets.

The N_2 adsorption–desorption isotherms of the V_2O_5 NS and rGO/V_2O_5 NS powders are shown in Figure S3. The V_2O_5 NS had a BET surface area of 8.4 m^2 g^{-1} and rGO/ V_2O_5 NS had the surface area of 36.2 m^2/g. The surface area of the rGO/V_2O_5 NS is 4 times higher than the V_2O_5 NS is could be due to the restacking of V_2O_5 NS is prevented by the rGO layers. The room temperature electrical conductivity was measured using the 4- probe technique. The conductivity of the V_2O_5 NS and the rGO/V_2O_5 NS was found to be 0.07 S/cm (Sheet resistance, R_s= 0.9 kΩ/sq) and 0.2 S/cm (Sheet resistance, R_s= 0.2 kΩ/sq), respectively. This conductivity is higher

than the vapour phase deposited V_2O_5[49] and rf-sputtered V_2O_5[50], but in the range of reported for

V_2O_5 gels.[51-52] The high conductivity of V_2O_5 NS is believed to occur via hopping of electron

between V^{5+} and V^{+4} impurity centers.[52] In comparison, the conductivity of the rGO/V_2O_5 NS is

more than twice that of the V_2O_5 NS due to the presence of the rGO nanosheets.

3.2. Electrochemical Characterization of the V_2O_5 Based Layered Electrodes

The V_2O_5 NS and rGO/V_2O_5 NS were investigated as cathodes for supercapacitor applications

using a three-electrode configuration set-up. The cyclic voltammetry curves (CVs) were

measured in the potential range of 0-0.8 V versus Ag/AgCl at different scan rates. As shown in

Figure 6a, the CVs of V_2O_5 NS electrodes show redox peaks which correspond to the

intercalation and de-intercalation of K^+ ion into/out of the V_2O_5 lattice, associated with the

different valence states of V_2O_5 orthorhombic structure.[35] The electrochemical intercalation of

K^+ into the V_2O_5 lattice is represented by the following equation

$V_2O_5 + xK^+ + xe^-$ …………………… $K_xV_2O_5$

Where, x is the mole fraction of inserted K^+ ions.

The redox activity of the V_2O_5 was significantly enhanced in the case of composites

containing both V_2O_5 and rGO nanosheets (rGO/V_2O_5 NS), as shown in Figure 6b. In fact, four

reversible redox peaks are clearly evident which are corresponding to the faradic redox activity

of V_2O_5. The increase in redox activity of rGO/V_2O_5 NS could be due to the increase in

conductivity of the V_2O_5 caused by the rGO layers. The shape synergetic effect of 2D

morphology of V_2O_5 nanosheets and 2D rGO sheets results in higher intimate contact with each

other, leading to the higher conductivity of the composite. The peak current increases with

increase in scan rate and negligible shift in the peak position with the scan rate is observed,

indicating that the redox reactions are quite reversible. The galvanostatic charge-discharge

studies were carried out to evaluate the capacitances in aqueous 1M KCl at different current densities and are shown in Figure 6c-d. The curvature of the charge-discharge curves indicates the dual contribution of the electrical double layer capacitance and pseudocapacitance. The discharge capacitance was found to be 635 F/g and 253 F/g for rGO/V_2O_5 NS and V_2O_5 NS at 1 A/g, respectively. The capacitance decrease with increasing current densities (Figure 7) could be due to the charge transport limitations. The increase in capacitance is due to the combined effect of high surface area as well high conductivity of the rGO/V_2O_5 NS. We note that these specific capacitance values are higher than many of those reported so far: V_2O_5 spheres (566 F/g, 5 mV/s),[38] atomic layer deposited V_2O_5/CNT composites (600 F/g, 5 mV/s),[53] V_2O_5/carbon nanofibers composites (150 F/g, 1mA/cm^2),[34] Nickel doped V_2O_5 thin films (417 F/g, 5 mV/s)[33] and rGO/V_2O_5 xerogels (195.4 F/g, 1 A/g).[37]

3.3. Asymmetric Supercapacitors Using V_2O_5 Based Layered Electrodes

Asymmetric supercapacitors have several advantages over symmetrical supercapacitors. The asymmetric supercapacitors utilizes the faradic activity cathode (energy source), which significantly contributes to the pseudocapacitance besides increasing the operating voltage window. Therefore, high energy density supercapacitors can be realized by asymmetric supercapacitor configuration. In our studies shown earlier, we demonstrated that the V_2O_5 layered electrodes show high faradaic activity at positive potential window between 0 to 0.8 V vs Ag/AgCl, and hence decided to use it as a cathode in an asymmetric supercapacitor device.

The electrochemcial characterization of rGO electrode was carried out using CV and galvanostatic charge-discharge techniques in 1 M KCl solution as shown in Figure S5. The rGO shows the potential window of 0 to -0.8 V was used as anode. The capacitance of 124 F/g was

obtained at 1 A/g and the capacitance decreases with increasing current density and attains a value of 86 F/g at 30 A/g.

We constructed two types of asymmetric supercapacitor devices. In one case V_2O_5 NS was used as cathode and activated rGO nanosheets was used as anode. In another device, rGO/V_2O_5 NS composite was used as cathode, and activated rGO nanosheets was used as anode. A 1M KCl electrolyte was used in both device types. The unit weight of the active materials of the cathode and anode exhibits different charge storage performance in 3-electrode configuration and therefore, to achieve the highest capacitance of the asymmetric supercapacitor, the charge balance ($q_+ = q_-$) of the cathode and anode had to be carefully maintained by using the appropriate masses of the two electrodes. The working operating potential window of the 2-electrode asymmetric device was 0 to 1.6 V compared to a working potential window of $0 - 0.8$ V vs. Ag/AgCl of the single electrode (3- electrode configuration).

To establish the appropriate potential window of operation of the asymmetric supercapacitors, a series of CVs (Figure 8a-b) were recorded at different potential windows. The current increases with increasing potential up to 1.6 V followed by decrease with further increase in potential to 1.7 V. Hence, the potential window of 0-1.6 V was chosen to characterize the asymmetric design of the supercapacitor.

Figure 8c-d shows the CV curves of asymmetric devices at different scan rates. These CV curves show that with increasing scan rate, currents and curvature of CV curves increase which indicates that both EDLC as well as pseudocapacitance effects contribute to the current. It can be seen that the currents of devices using rGO/V_2O_5 NS composite electrodes are higher than the devices using V_2O_5 NS devices. In addition, the redox peaks are more prominent with

rGO/V$_2$O$_5$ NS composite electrodes, which may be due to the higher conductivity of the rGO/V$_2$O$_5$ NS composite.

To evaluate the cell capacitance, galvanostatic charge-discharge measurements were performed at different current densities with the potential window of 0-1.6 V (Figure 9a-b). The cell capacitance was calculated by considering the active mass of both cathode and anode electrodes. The maximum cell capacitance of 195 F/g and 95 F/g was achieved at 1A/g for the rGO/V$_2$O$_5$ NS and V$_2$O$_5$ NS supercapacitors, respectively. The capacitance decreases with increasing current density (Figure 9c) and reach of 54 F/g and 7.5 F/g at 30 A/g. The energy density (E) and power density of the supercapacitors were calculated using following equations: $E = 1/2 C_{sp}(\Delta V)^2$ and $P = E/\Delta t$, where C_{sp} is specific capacitance, ΔV is the potential window and Δt is the discharge time of the supercapacitor. Figure 9d shows the Ragone plot of the asymmetric supercapacitors. It can be seen that an energy density of 75.9 Wh/kg and 39 Wh/kg were achieved for rGO/V$_2$O$_5$ NS and V$_2$O$_5$ NS NS supercapacitors, respectively at a power density of 900 W/kg. The energy densities are higher than those reported for the Ppy@V$_2$O$_5$ nanoribbon composite (32 Wh/kg, 900 W/kg),[26] V$_2$O$_5$ nanofibers and polyaniline nano fibers (26.7 wh/kg, 222 W/kg),[35] graphite nanoplatelets-V$_2$O$_5$ nanocomposite (28 Wh/kg, 303 W/kg),[50] graphene composites of V$_2$O$_5$ nanowires and MnO$_2$ nanorods (15.4 Wh/kg, 436 W/kg)[25] etc asymmetric supercapacitors.

The electrochemical impedance spectra of asymmetric supercapacitors of V$_2$O$_5$ NS and rGO/V$_2$O$_5$ NS were measured in aqueous 1 M KCl at open-circuit potentials in the frequency range of 1 MHz to 0.1 Hz (Figure 10). The Nyquist plot consists of semicircle followed by Warburg impedance. The impedance spectra were fitted into an equivalent circuit comprising of solution resistance (ohmic resistance of the electrolyte and internal resistance of the electrode

materials, Rs) is in series with the parallel combination of double layer capacitance (Cdl) and interfacial charge-transfer resistance (R_{ct}) and a warburg impedance (W). The solution resistance (8.5 Ω) for the V_2O_5 NS and rGO/V_2O_5 NS devices is almost same, as these are measured in the same electrolyte testing medium. On the other hand, the R_{ct} for the V_2O_5 NS and rGO/V_2O_5 NS were found to be 15.5 and 12.5 Ω, respectively. The better kinetics of the rGO/V_2O_5 NS could be due to the high conductivity of the composite electrode. The low frequency capacitance spectra are inclined at an angle to the real axis, implying that the capacitance is associated with resistance. The stability of the asymmetric supercapacitors of V_2O_5 NS and rGO/V_2O_5 NS are shown in the Figure 11. It can be seen that the capacitance retention after 3000 cycles for asymmetric supercapacitors of rGO/V_2O_5 NS (94%) is higher than the V_2O_5 NS (92%).

4. Conclusions

We have synthesized 2D layered electrode hetrostructures with high Faradaic activity and applied them in aqueous asymmetric supercapacitor devices. The electrodes are based on 2D rGO/V_2O_5 NS with high intimate contact, which improves the conductivity of the composite electrode. The energy density of 75.9 Wh/kg were achieved for rGO/V_2O_5 NS electrodes at a power density of 900 W/kg. The energy density and power densities of these devices are, to our knowledge, higher than any reported for asymmetric supercapacitors utilizing V_2O_5 as electrodes.

Acknowledgements

References:

1   G. Wang, L. Zhang and J. Zhang, *Chem. Soc. Rev.*, 2012, **41**, 797-828.

2   W. Wei, X. Cui, W. Chen and D. G. Ivey, *Chem. Soc. Rev*, 2011, **40**, 1697-1721.

3   S. W. Zhang and G. Z. Chen, *Ener. Mater.: Mater. Sci. Eng.Ener. Sys.*, 2008, **3**, 186-200.

4   Y. M. Vol'fkovich and T. M. Serdyuk, *Russian J. Electrochem.*, 2002, **38**, 935-958.

5   A. L. M. Reddy, S. R. Gowda, M. M. Shaijumon and P. M. Ajayan, *Adv. Mater.*, 2012, **24**, 5045-5064.

6   J. Yan, Q. Wang, T. Wei and Z. Fan, *Adv. Ener. Mate.*, 2014, **4**, 1300816- 1300840.

7   F. Wang, S. Xiao, Y. Hou, C. Hu, L. Liu and Y. Wu, *RSC Adv.*, 2013, **3**, 13059-13084.

8   W. Tang, Y. Y. Hou, X. J. Wang, Y. Bai, Y. S. Zhu, H. Sun, Y. B. Yue, Y. P. Wu, K. Zhu and R. Holze, *J. Power Sources*, 2012, **197**, 330-333.

9   W. Tang, L. Liu, S. Tian, L. Li, Y. Yue, Y. Wu and K. Zhu, *Chem. Commun.*, 2011, **47**, 10058-10060.

10   Z. Fan, J. Yan, T. Wei, L. Zhi, G. Ning, T. Li and F. Wei, *Adv. Funct. Mater.*, 2011, **21**, 2366-2375.

11   H. Wang, Y. Liang, T. Mirfakhrai, Z. Chen, H. Casalongue and H. Dai, *Nano Res.*, 2011, **4**, 729-736.

12   Y. Xue, Y. Chen, M.-L. Zhang and Y.-D. Yan, *Mater. Lett.*, 2008, **62**, 3884-3886.

13   T. Brousse, P.-L. Taberna, O. Crosnier, R. Dugas, P. Guillemet, Y. Scudeller, Y. Zhou, F. Favier, D. Bélanger and P. Simon, *J. Power Sources*, 2007, **173**, 633-641.

14   G. Yu, L. Hu, M. Vosgueritchian, H. Wang, X. Xie, J. R. McDonough, X. Cui, Y. Cui and Z. Bao, *Nano Lett.*, 2011, **11**, 2905-2911.

15   Z.-S. Wu, W. Ren, D.-W. Wang, F. Li, B. Liu and H.-M. Cheng, *ACS Nano*, 2010, **4**, 5835-5842.

16   H. Wang, C. B. Holt, Z. Li, X. Tan, B. Amirkhiz, Z. Xu, B. Olsen, T. Stephenson and D. Mitlin, *Nano Res.*, 2012, **5**, 605-617.

17   N. Yu and L. Gao, *Electro. Commun.*, 2009, **11**, 220-222.

18   Z. Chen, D. Weng, H. Sohn, M. Cai and Y. Lu, *RSC Adv.*, 2012, **2**, 1755-1758.

19   B. Jin, Q. Yan and Y. Dou, *Recent Pat. Mater. Sci.*, 2012, **5**, 199-212.

20   S. W. Zhang and G. Z. Chen, *Ener. Mater.*, 2008, **3**, 186-200.

21.   C. D. Lokhande, D. P. Dubal and O.-S. Joo, *Curr. Appl. Phys.*, 2011, **11**, 255-270.

22   W. Deng, X. Ji, Q. Chen and C. E. Banks, *RSC Adv.*, 2011, **1**, 1171-1178.

23   X. Zhao, B. M. Sanchez, P. J. Dobson and P. S. Grant, *Nanoscale*, 2011, **3**, 839-855.

24   S. D. Perera, A. D. Liyanage, N. Nijem, J. P. Ferraris, Y. J. Chabal and K. J. Balkus Jr, *J. Power Sources*, 2013, **230**, 130-137.

25   S. D. Perera, M. Rudolph, R. G. Mariano, N. Nijem, J. P. Ferraris, Y. J. Chabal and K. J. Balkus, *Nano Ener.*, 2013, **2**, 966-975.

26   Q. Qu, Y. Zhu, X. Gao and Y. Wu, *Adv. Ener. Mater.*, 2012, **2**, 950-955.

27   X. Rui, Z. Lu, Z. Yin, D. H. Sim, N. Xiao, T. M. Lim, H. H. Hng, H. Zhang and Q. Yan, *Small*, 2013, **9**, 716-721.

28   I. Shakir, J. H. Choi, M. Shahid, S. A. Shahid, U. A. Rana, M. Sarfraz and D. J. Kang, *Electrochim. Acta*, 2013, **111**, 400-404.

29   H. Zhang, A. Xie, C. Wang, H. Wang, Y. Shen and X. Tian, *ChemPhysChem*, 2013.

30   H. Zhao, L. Pan, S. Xing, J. Luo and J. Xu, *J. Power Sources*, 2013, **222**, 21-31.

31   H. Zhao, L. Pan, S. Xing, J. Luo and J. Xu, *J. Power Sources*, 2013, **222**, 21-31.

32   K. Jeyalakshmi, S. Vijayakumar, S. Nagamuthu and G. Muralidharan, *Mater. Res. Bull.*, 2013, **48**, 760-766.

33   K. Jeyalakshmi, S. Vijayakumar, K. K. Purushothaman and G. Muralidharan, *Mater. Res. Bull.*, 2013, **48**, 2578-2582.

34   B. H. Kim, K. S. Yang and D. J. Yang, *Electrochim. Acta*, 2013, **109**, 859-865.

35   Q. T. Qu, Y. Shi, L. L. Li, W. L. Guo, Y. P. Wu, H. P. Zhang, S. Y. Guan and R. Holze, *Electrochem. Commun.*, 2009, **11**, 1325-1328.

36   G. Wee, H. Z. Soh, Y. L. Cheah, S. G. Mhaisalkar and M. Srinivasan, *J. Mate. Chem.*, 2010, **20**, 6720-6725.

37   J. Xu, H. Sun, Z. Li, S. Lu, X. Zhang, S. Jiang, Q. Zhu and G. S. Zakharova, *Solid State Ionics*, 2013.

38   J. Yang, T. Lan, J. Liu, Y. Song and M. Wei, *Electrochim. Acta*, 2013, **105**, 489-495.

39   L. M. Chen, Q. Y. Lai, Y. J. Hao, Y. Zhao and X. Y. Ji, *J. Alloys Compd.*, 2009, **467**, 465-471.

40   J. H. Huang, Q. Y. Lai, J. M. Song, L. M. Chen and X. Y. Ji, *Chin. J. Inorg. Chem.*, 2007, **23**, 237-242.

41   M. Jayalakshmi, M. M. Rao, N. Venugopal and K. B. Kim, *J. Power Sources*, 2007, **166**, 578-583.

42   T. Kudo, Y. Ikeda, T. Watanabe, M. Hibino, M. Miyayama, H. Abe and K. Kajita, *Solid State Ionics*, 2002, **152-153**, 833-841.

43   H. Y. Lee and J. B. Goodenough, *J. Solid State Chem.*, 1999, **148**, 81-84.

44   K. W. Nam, S. B. Ma, W. S. Yoon, X. Q. Yang and K. B. Kim, *Electrochem. Commun.*, 2009, **11**, 1166-1169.

45   J. Zhu, L. Cao, Y. Wu, Y. Gong, Z. Liu, H. E. Hoster, Y. Zhang, S. Zhang, S. Yang, Q.

       Yan, P. M. Ajayan and R. Vajtai, *Nano Lett.*, 2013, **13**, 5408-5413.

46   R. Baddour-Hadjean, V. Golabkan, J. P. Pereira-Ramos, A. Mantoux and D. Lincot, *J.

       Raman Spec.*, 2002, **33**, 631-638.

47   N. Kurra, V. S. Bhadram, C. Narayana, and G. U. Kulkarni, *ACS Appl. Mater. Interfaces*

       2012, **4**, 1030−1036.

48   N. Pinna, M. Willinger, K. Weiss, J. Urban and R. Schlögl, *Nano Lett.*, 2003, **3**, 1131-

       1134.

49   T. Allersma, R. Hakim, T. N. Kennedy, J. D. Mackenzie, *J. Chem. Phys.* 1967, **46**,   154

       160.

50   F. P. Koffyberg, F. A. Benko, *Philos. Mag. B* 1978, **38**, 357-366.

51   J. Bullot, O. Gallais, M. Gauthier, J. Livage, *Appl. Phys. Lett.* 1980, **36**, 986-988.

52   R. Maoz, E. Frydman, S. R. Cohen, J. Sagiv, *Adv. Mater.* 2000, **12**, 420-424.

53   S. Boukhalfa, K. Evanoff, G. Yushin, *Ener. Environ. Sci.* 2012, **5**, 6872-6879.

Graphical Abstract
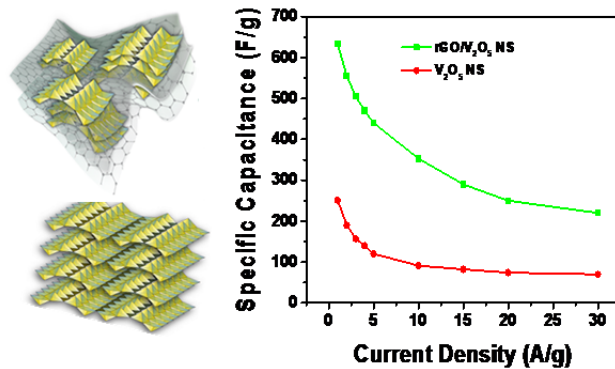
The 2D layered heterostructures of V_2O_5 nanosheets and reduced graphene oxide show high conductivity and superior asymmetric supercapacitor properties.
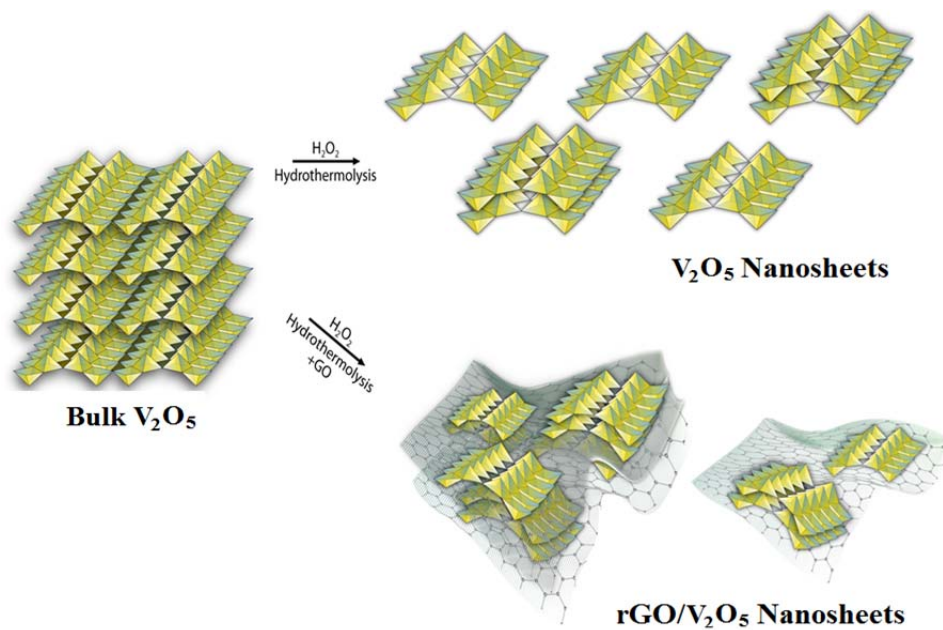
Figure 1. Schematic process of the hydrothermal synthesis of V_2O_5 NS and rGO/V_2O_5 NS.
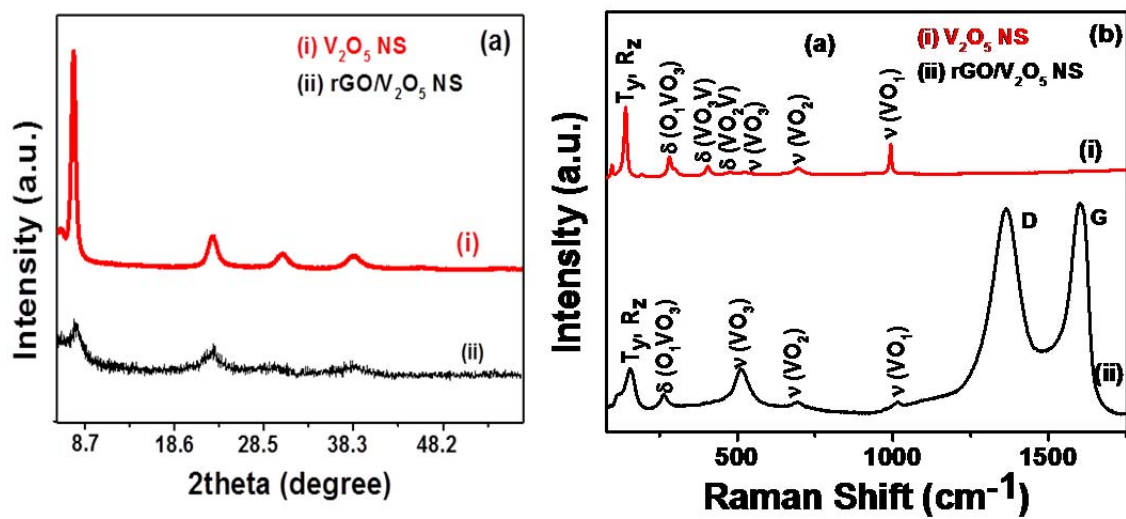
Figure 2. (a) XRD patterns of (i) V_2O_5 NS and (ii) rGO/V_2O_5 NS (a), (b) Raman spectra of (i) V_2O_5 NS and (ii) rGO/V_2O_5 NS.
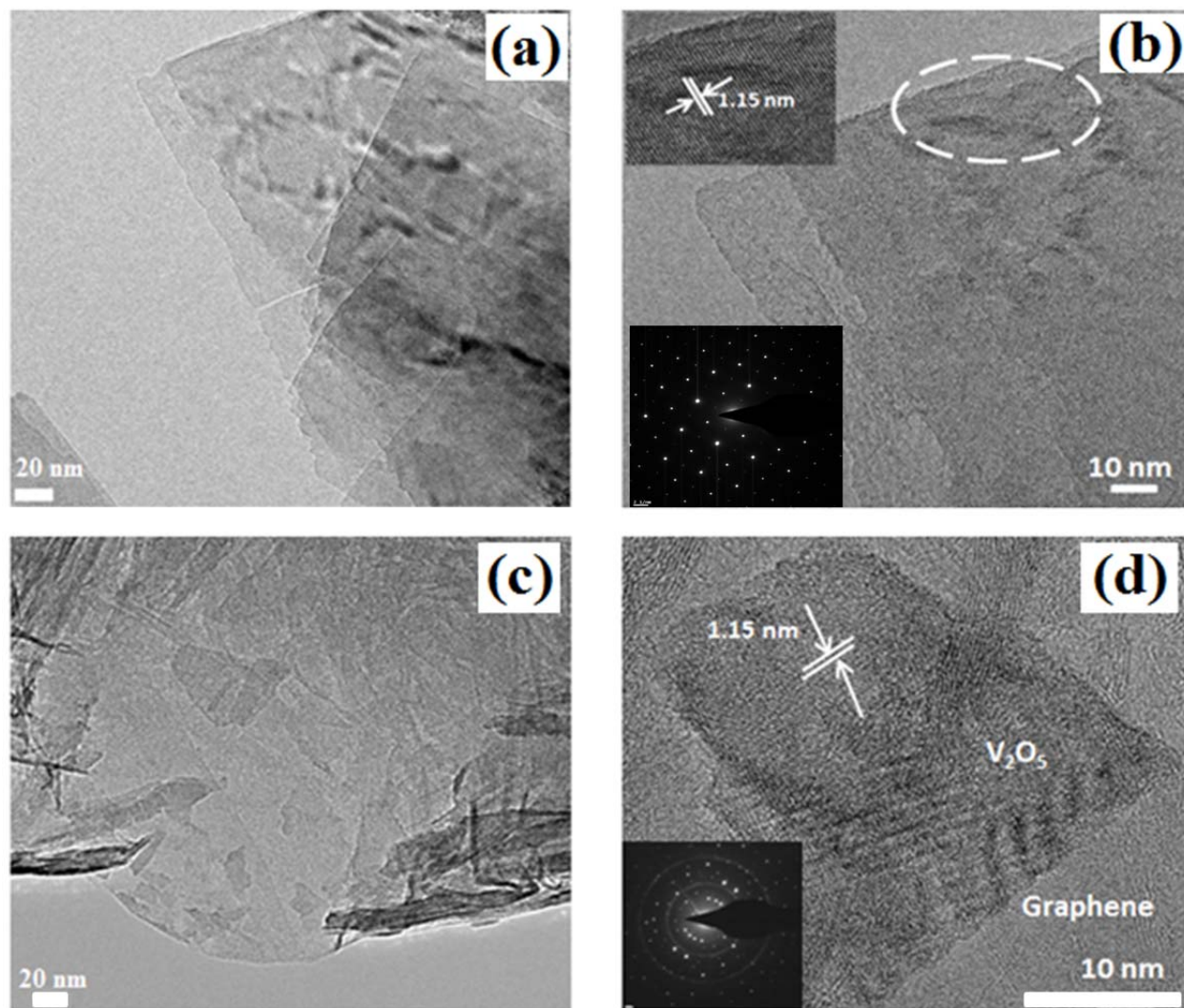
Figure 3. TEM images of (a) V_2O_5 NS and (b) rGO/V_2O_5 NS and (c & d), their corresponding high resolution images. Inset of (b) is the zoomed portion of the circular region showing the lattice fringes. The diffraction patterns are shown in the inset of (b) and (d).
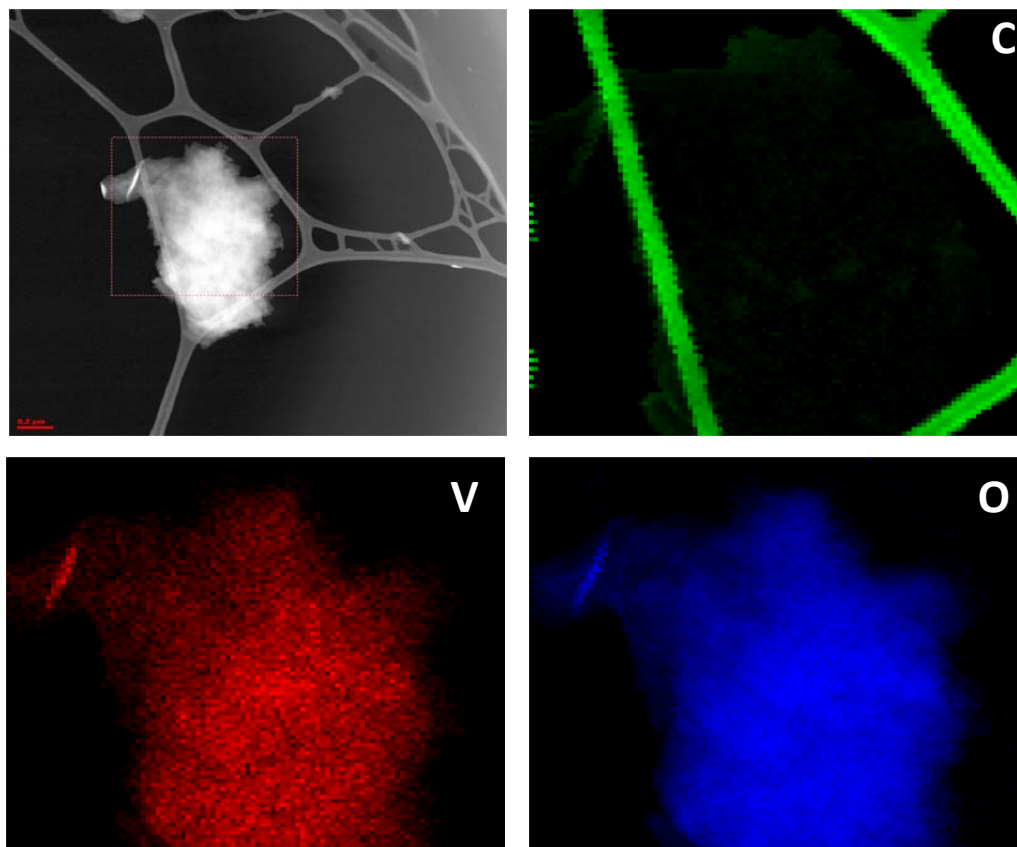
Figure 4. STEM images of V_2O_5 NS and their corresponding zoomed portion EELS mapping of carbon (C), vanadium (V) and oxygen (O) images. The green lines from the elemental mapping originated from the carbon coated TEM copper grid.
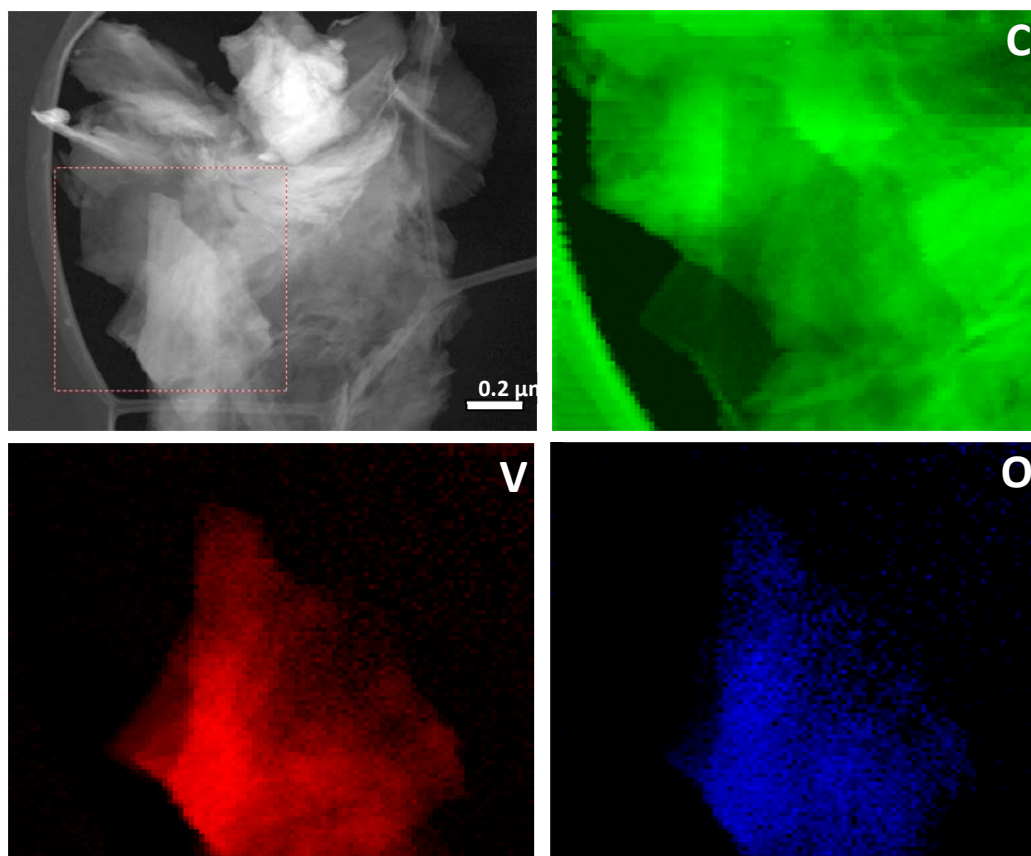
Figure 5. STEM images of rGO/V$_2$O$_5$ NS and their corresponding zoomed portion EELS mapping of carbon (C), vanadium (V) and oxygen (O) images.
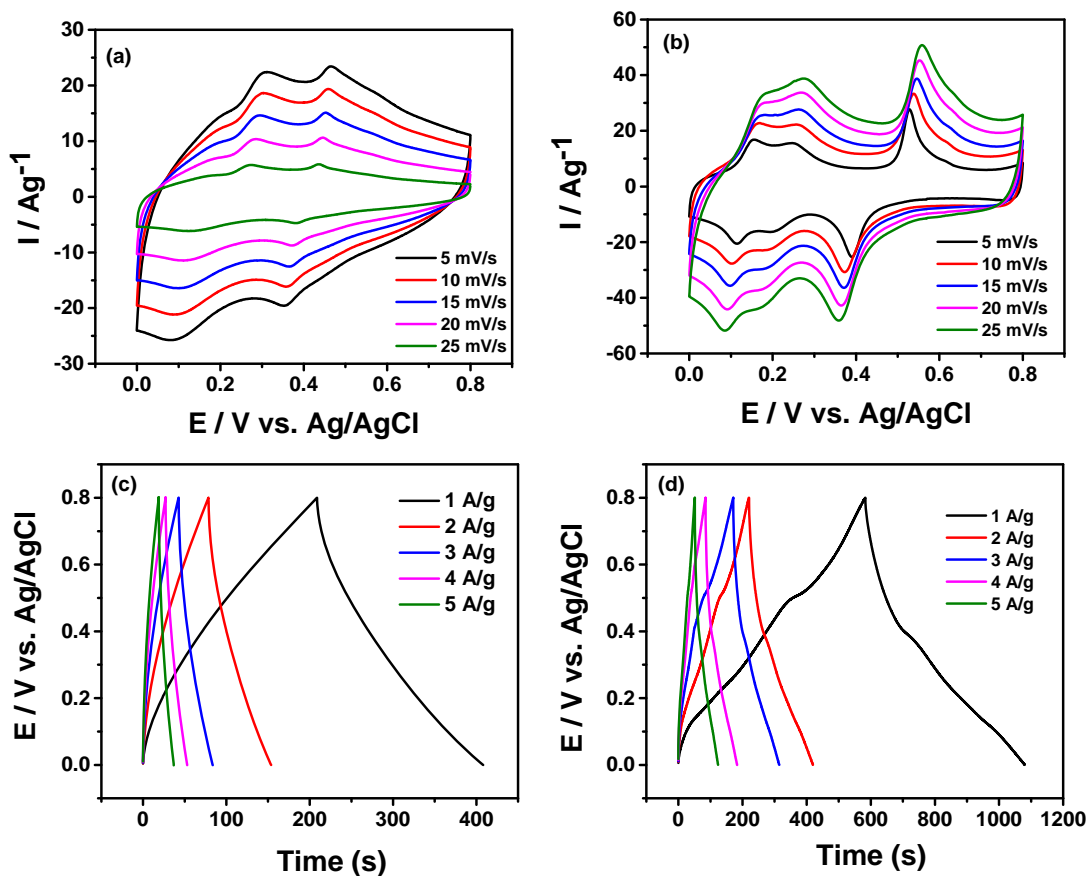
Figure 6. Cyclic voltammograms at different scan rates of V_2O_5 NS and rGO/V_2O_5 NS (a-b) their corresponding galvanostatic charge-discharge plots (c-d) at different current densities in aqueous 1 M KCl solution.
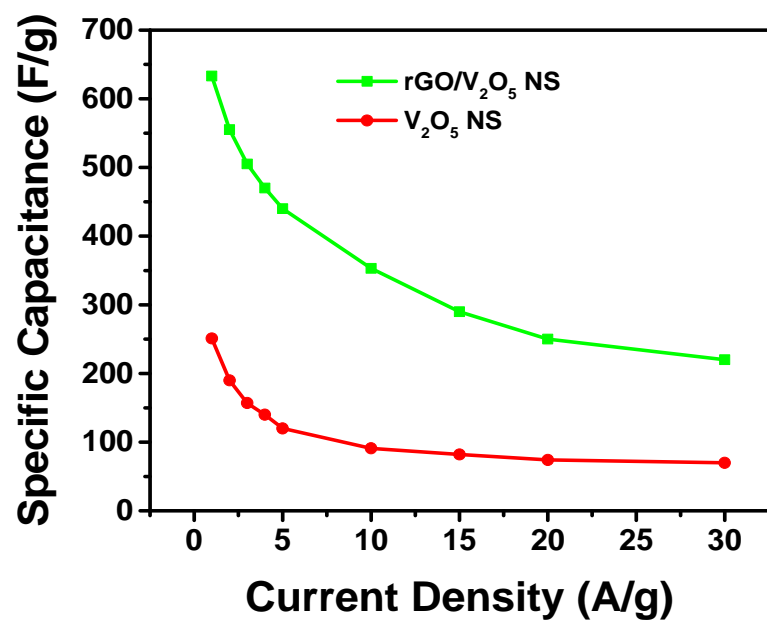
Figure 7. Plot of specific capacitance versus current density of V_2O_5 NS and rGO/V_2O_5 NS
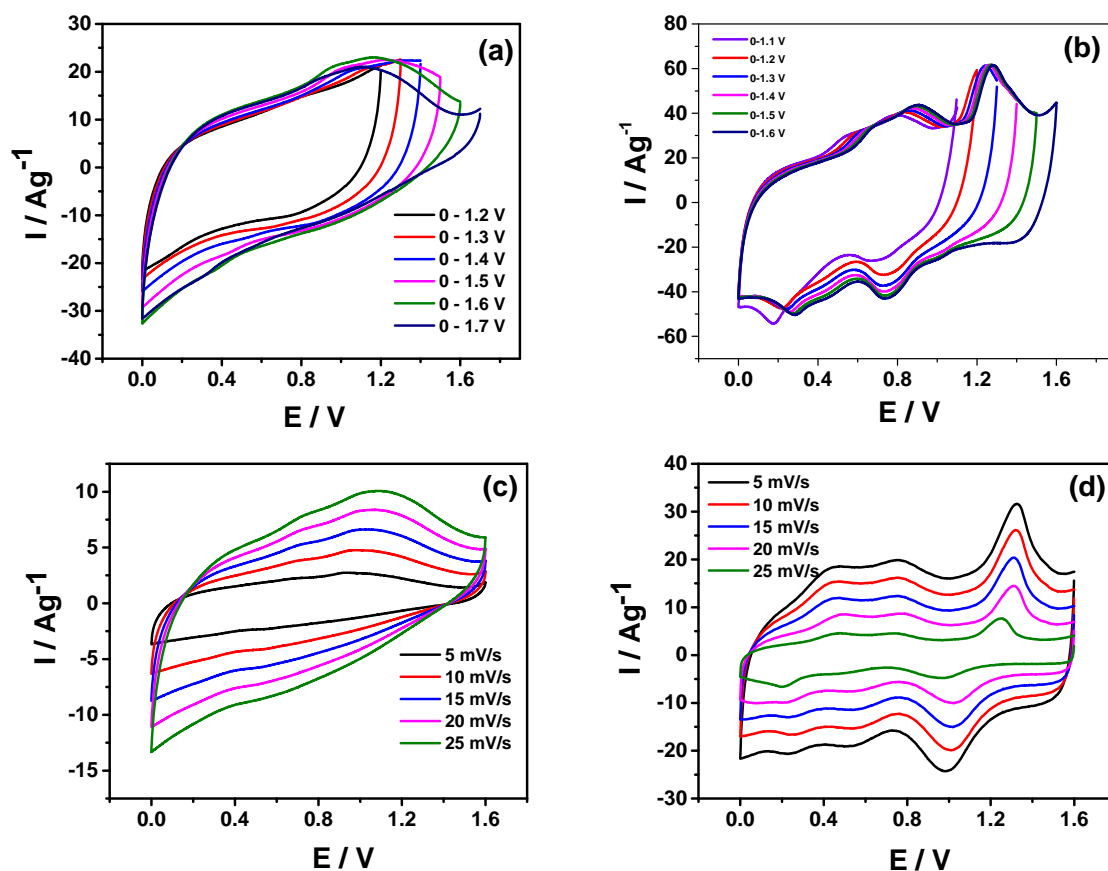
Figure 8. CVs of V_2O_5 NS (a), rGO/V_2O_5 NS supercapacitors (b) measured in aqueous 1 M KCl at different potential windows at a scan rate of 50 mV/s, CVs at different scan rates of V_2O_5 NS (c), rGO/V_2O_5 NS supercapacitors (d) in aqueous 1 M KCl solution.
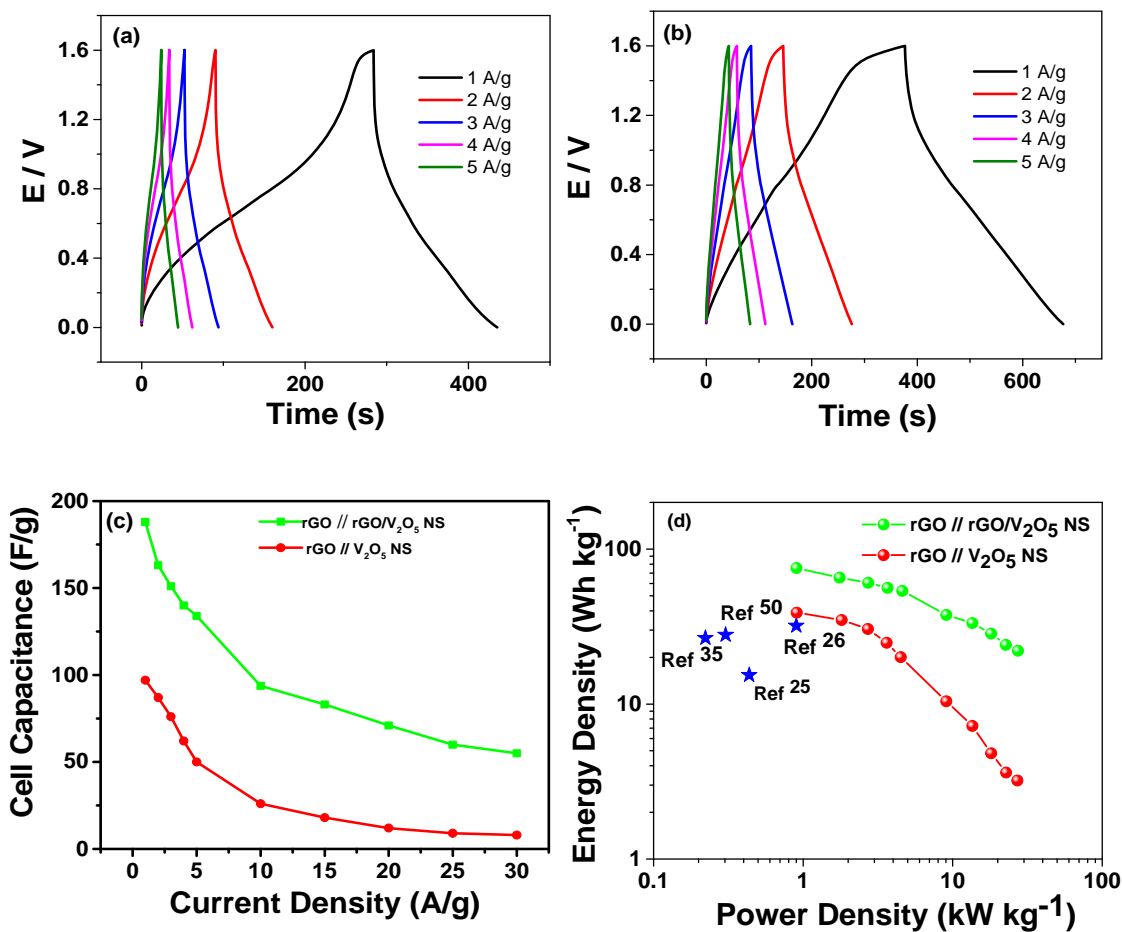
Figure 9. Galvanosttic charge-discharge plots measured at different current densities in aqueous 1 M KCl solution of (a) V_2O_5 NS (b) rGO/V_2O_5 NS (c) cell capacitance versus current density for the corresponding asymmetric supercapacitors, and (d) Ragone plots.
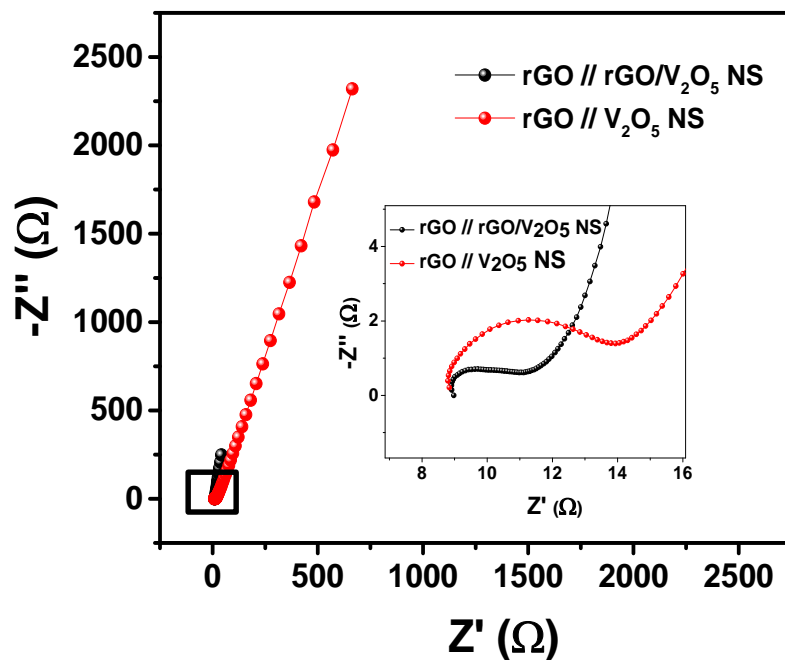
Figure 10. EIS Nyquist plots for the V_2O_5 NS and rGO/V_2O_5 NS electrodes used in asymmetric supercapacitors measured in 1 M KCl solution at a DC bias voltage of 0 V with ac amplitude of 10 mV. The inset is the zoomed portion of the high frequency region.
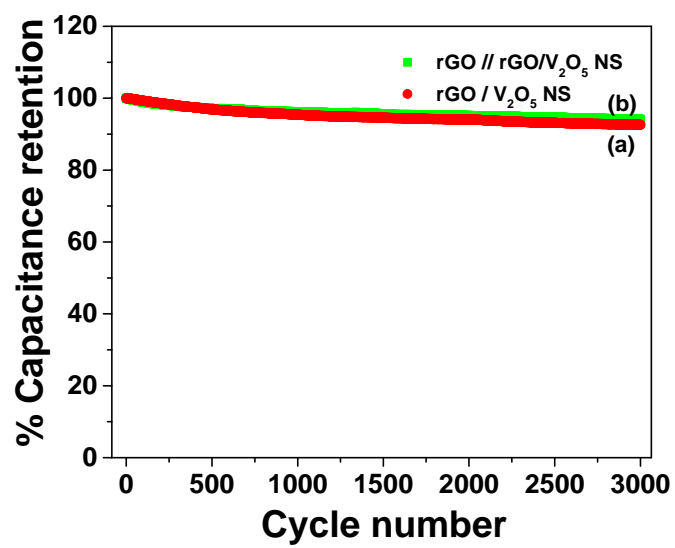
Figure 11. Plot of capacitance versus cycle number of (a) V_2O_5 NS and (b) rGO/V_2O_5 NS

Supporting Information

Two-Dimensional Heterostructures of V_2O_5 Nanosheets and Reduced Graphene Oxide as Electrodes for High Energy Density Asymmetric Supercapacitors

D. H. Nagaraju, Muhammad Shahid, Qingxiao Wang, P. Beaujuge, and H. N. Alshareef[*]
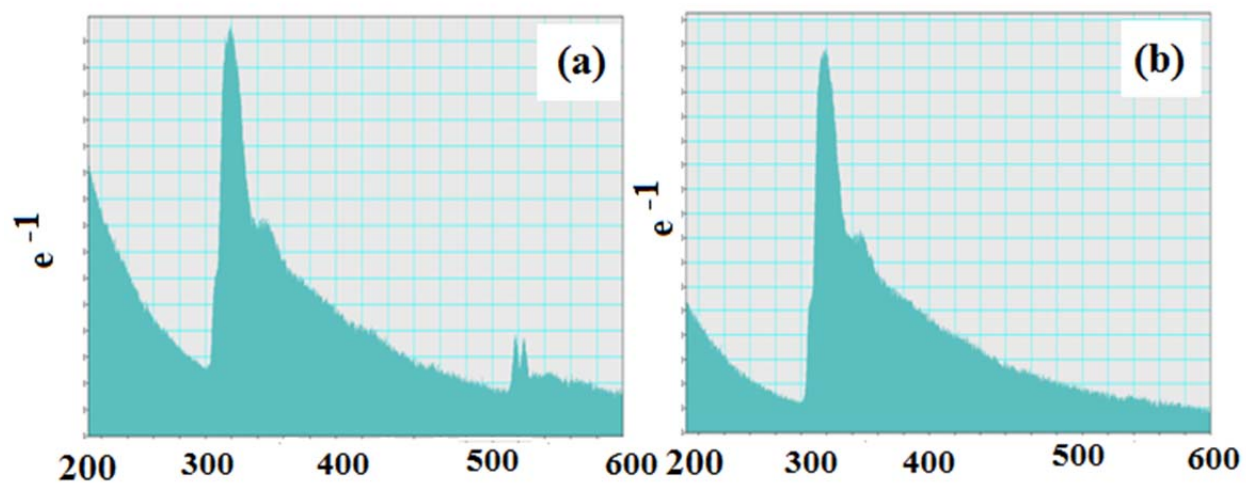
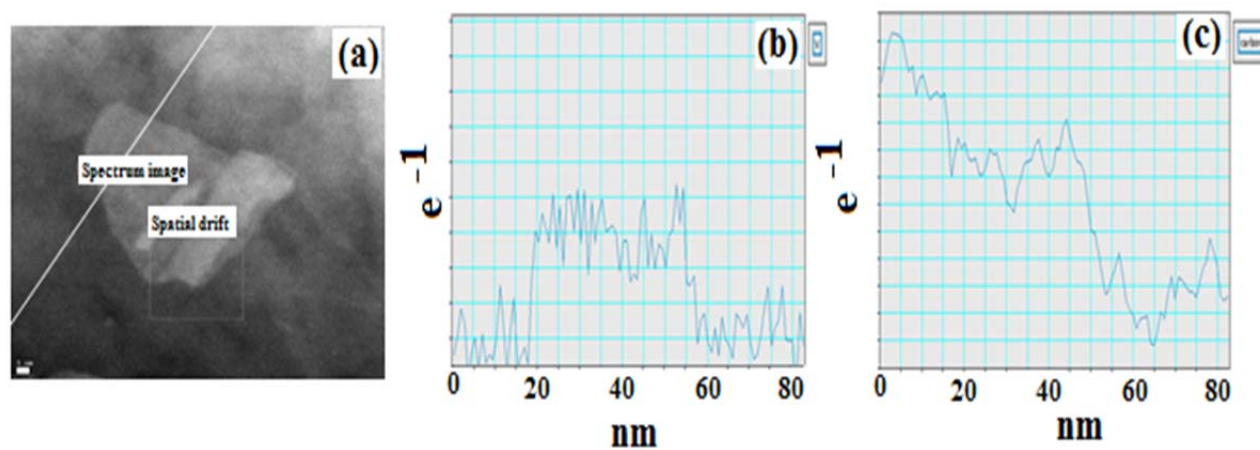**Figure S1.** EELS spectra of (a) rGO/V_2O_5 NS composite and (b) only on graphene region

Figure S2. STEM image of the rGO/V$_2$O$_5$ NS (a), line spectrum on V$_2$O$_5$ NS region (b) and line spectrum on graphene region (c)
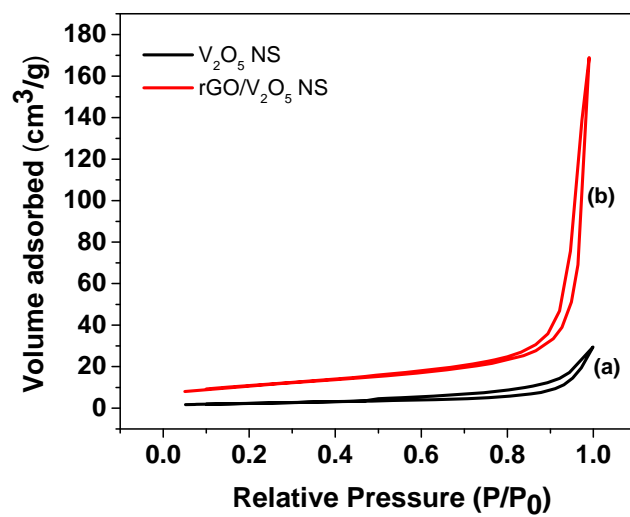
Figure S3. N_2 adsorption-desorption isotherms of (a) V_2O_5 NS and (b) rGO/V_2O_5 NS.
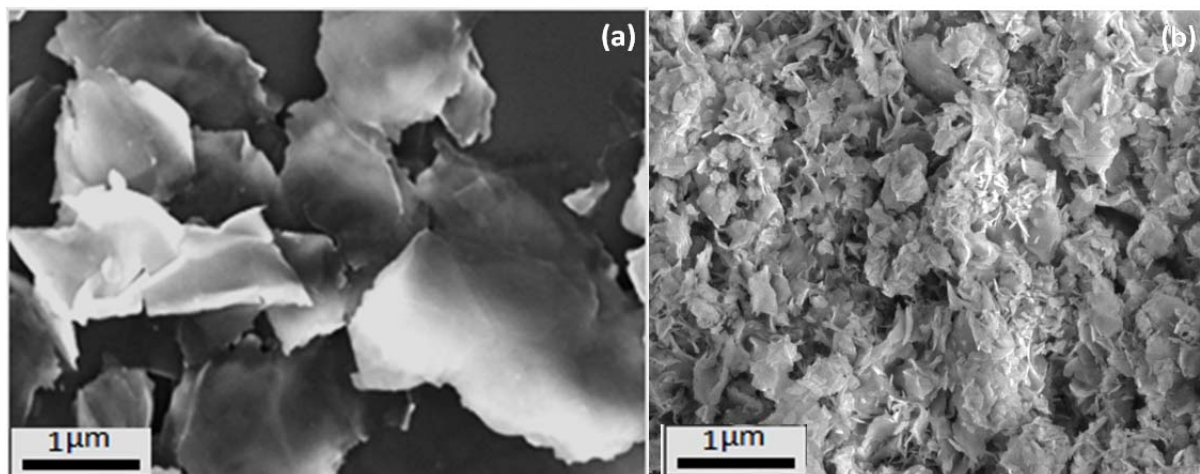
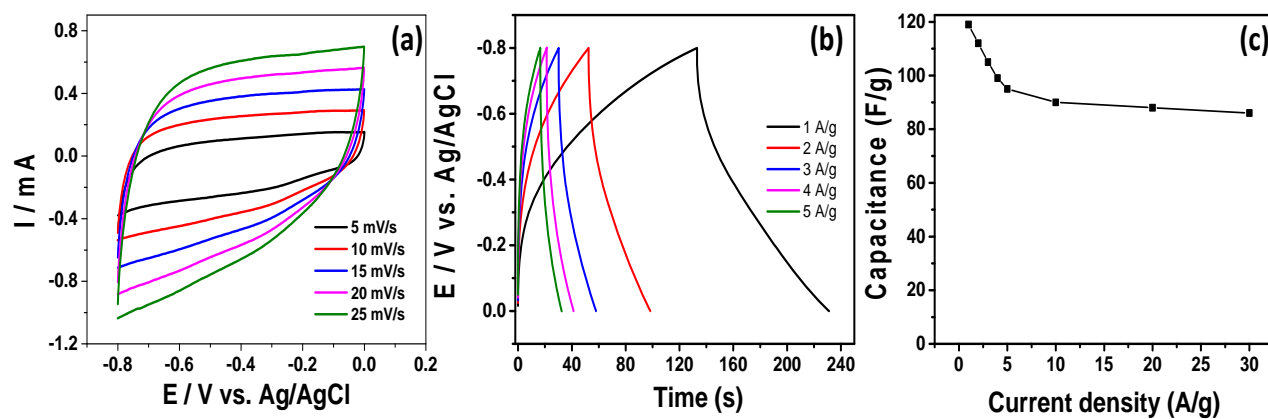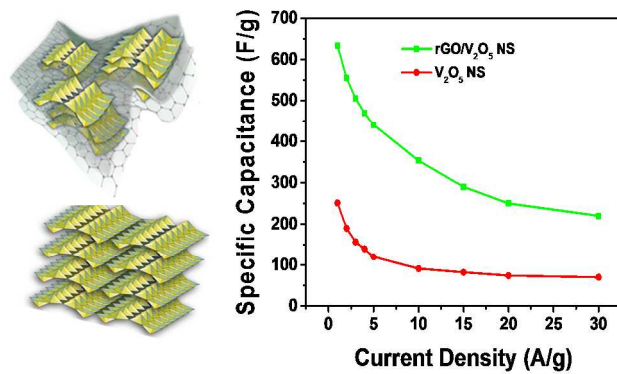**Figure S4.** SEM imges of the (a) V2O5 NS and (b) rGO/V2O5 NS.

Figure S5. CVs of (a) rGO in 1 M KCl at different scan rates (b) galvanostatic charge-discharge charactristics at diferent current densities and (c) the plot of variation of capacitance with current density.

Graphical Abstract

The 2D layered heterostructures of V_2O_5 nanosheets and reduced graphene oxide show high conductivity and superior asymmetric supercapacitor properties.